OPEN ACCESS
JOURNAL OF ADVANCED DIELECTRICS
Vol. 11, No. 6 (2021) 2150028 (9 pages)

DOI: 10.1142/S2010135X21500284

Effect of sintering temperature on structural, magnetic, dielectric and optical properties of Ni–Mn–Zn ferrites

Nazia Khatun*, Mohammad Sajjad Hossain*,§, Most. Hosney Ara Begum*, Suravi Islam*, Nazmul Islam Tanvir*, Riyadh Hossen Bhuiyan† and Md. Al-Mamun‡

*Industrial Physics Division, Bangladesh Council of Scientific and Industrial Research (BCSIR) Dhaka 1205, Bangladesh

†Fiber and Polymer Division, Bangladesh Council of Scientific and Industrial Research (BCSIR) Dhaka 1205, Bangladesh

‡Atomic Energy Centre (AEC), Dhaka 1000, Bangladesh

§sajjadbcsir@gmail.com

Received 23 July 2021; Revised 7 October 2021; Accepted 28 October 2021; Published 30 November 2021

Spinel ferrite $Ni_{0.08}Mn_{0.90}Zn_{0.02}Fe_2O_4$ was prepared by a conventional ceramic process followed by sintering at three different temperatures (1050°C, 1100°C and 1150°C). X-ray diffraction (XRD) investigations stated the single-phase cubic spinel structure and the FTIR spectra revealed two prominent bands within the wavenumber region from 600 cm^{-1} to 400 cm^{-1}. Surface morphology showed highly crystalline grain development with sizes ranging from 0.27 μm to 0.88 μm. The magnetic hysteresis curve at ambient temperature revealed a significant effect of sintering temperature on both coercivity (H_c) and saturation magnetization (M_s). Temperature caused a decrease in DC electrical resistivity, while the electron transport increased, suggesting the semiconducting nature of all samples and that they well followed the Arrhenius law from which their activation energies were determined. The values of Curie temperature (T_c) and activation energy were influenced by the sintering temperature. Frequency-dependent dielectric behavior (100 Hz–1 MHz) was also analyzed, which may be interpreted by the Maxwell–Wagner-type polarization. The UV–vis–NIR reflectance curve was analyzed to calculate the bandgap of ferrites, which showed a decreasing trend with increasing sintering temperature.

Keywords: Ferrites; ceramic technique; FTIR; dielectric constant; hysteresis curve; bandgap.

1. Introduction

After the discovery of spinel ferrites, several basic and applied investigations extensively focused on the mechanisms of their synthesis and fabrication processes in order to enhance their physical characteristics. Also, their wider range of potential applications in various fields as well as insight physics made the researchers and engineers to be involved in the research on their various aspects. The chemical formula for a ferrite is $MO{\cdot}Fe_2O_3$, where M represents the divalent metal ion. In ferrite, this divalent metal ion (M^{2+}) occupies both tetrahedral (A) and octahedral (B) sites along with the trivalent ion (Fe^{3+}) which can be represented by the formula $(M_\delta Fe_{1-\delta})[M_{1-\delta}Fe_{1+d}]O_4$, where δ is known as the degree of inversion that signifies the occupancy of A- and B-sites by the cations.[1] The δ-value defines the disposition of cations in two different absolute cases. In the case of spinel structure ($\delta = 0$), entire A-sites are occupied by M^{2+} ions, whereas the B-sites are occupied by Fe^{3+} ions. On the other hand, in the inverse spinel structure ($\delta = 1$), all M^{2+} ions occupy the B-sites and Fe^{3+} cations are equally distributed between the A- and B-sites. For mixed structures, both A- and B-sublattices are shared by divalent (M^{2+}) and trivalent (Fe^{3+}) cations.[2] Ferrite possesses some fundamental and multiple diverse features including high magnetic and electrical properties, good thermal and chemical stabilities and mechanical stiffness, making them superior magneto-electric materials for applications in many devices.[3] Their high resistivity (~10^7–10^9 Ω·cm) at room temperature results in low eddy current losses at the high-frequency region, thus making them to be commonly used in most magnetic amplifiers, inductors, antenna rods, transformers and recording heads.[4] Apart from these applications, researchers in the past few years have focused their study on different potential fields. Reference 5 synthesized $Ni_{0.4}Zn_{0.2}Mn_{0.4}Fe_2O_4$ nanoferrite for radar absorbing device. Due to high values of Curie temperature and thermal stability, the EPR spectra showed reduction in the peak width and increase in relaxation with the increase in sintering temperature. These results exhibited that environmentally safe Ni–Mn–Zn ferrite particles can be used for absorbing electromagnetic (EM) emission produced by a radar from few MHz to 2 GHz. Low loss and high saturation magnetization proposed their potential application in microwave system as they decrease the emission of unwanted EM waves

§Corresponding author.

from the device and also absorb the incoming EM waves that may harm the microwave device.[6] Reference 7 described that the MnZn ferrite nanoparticles exhibiting high reflection loss and broad absorbing band in low frequency (10 MHz–1 GHz) can be used in the electromagnetic microwave absorbing field. A one-pot thermal decomposition method was used to synthesize a series of Zn-doped Mn ferrites with a particle size of ~15 nm possessing high magnetization value (175 emu/g), providing large MRI contrast effects ($r_2 = 860\ mm^{-1} \cdot s^{-1}$) with an 8–14-fold increase in MRI contrast and a fourfold enhancement in hyperthermic effects compared to conventional iron oxide.[8] Reference 9 has found the photocatalytic potential of sol–gel-based Mg–Mn–Zn ferrites against Chloramine T and Rhodamine B dyes as well their anti-biofilm activity towards pathogenic bacteria and *Candida* sp. Many researchers studied the influence of different additives or dopants on the structural, electrical and magnetic behaviors in the two main common kinds of ferrites; nickel–zinc (Ni–Zn) and manganese–zinc (Mn–Zn) ferrites.[10–13] Mn–Zn ferrites exhibit considerable initial permeability and magnetization, but their poor charge transportation and low dielectric losses make them undesirable for high-frequency magnetic applications. Contrarily, the Ni–Zn ferrites possess moderate permeability in the high-frequency regions, although they have high electrical resistivity and low dielectric losses.[14] In contrast to these ferrites, the combination of Ni–Zn and Mn–Zn ferrites, namely the Ni–Mn–Zn ferrites, may improve the magnetic characteristics and can be applicable at high-frequency regions. The permeability increases with the substitution of Zn for Ni in the Ni–Mn–Zn ferrites but the Curie temperature decreases at adequately high temperature due to Zn evaporation.[15] These properties are very important during the preparation, such as the sintering temperature and time duration apart from the additives.[16] The magnetic properties of ferrites are strongly influenced by their chemical composition, microstructure and sintering conditions.[17] Microstructural factors like density, grain size, boundary, porosity and inter-granular distribution can be controlled by the sintering temperature. Thus, sintering temperature plays a crucial role in manipulating the magnetic behavior.[18] Several techniques (e.g., sol–gel, citrate precursor, hydrothermal technique, micro-emulsion method, etc.) have been employed at various sintering conditions and their effects on the magnetic properties have been reported.[19–21] This study detailed the influence of sintering temperature on the structural, magnetic, dielectric and optical characteristics of $Ni_{0.08}Mn_{0.90}Zn_{0.02}Fe_2O_4$ which had not previously been reported. This work supplements the basic and applied research of ferrites, with emphasis on improving their physical properties.

2. Materials and Method

2.1. *Preparation*

Polycrystalline $Ni_{0.08}Mn_{0.90}Zn_{0.02}Fe_2O_4$ ferrite was synthesized by the conventional ceramic technique. Analytical-grade (99% pure; Merck, Germany) nickel oxide (2.585 g), manganese oxide (27.622 g), zinc oxide (0.7042 g) and iron (II) oxide (69.089 g) were stoichiometrically weighted and dried at 120°C for 1 h to remove the moisture content. All the raw materials were mixed in a planetary ball mill where ethanol was used as a wet medium to make a homogeneous slurry. Alumina balls were used to impede iron contamination. The weight ratio of ball to powder was 2:1. The powder was contained in an alumina bowl (250 mL) and pulverized at 150 rpm for 8 h. Then the powders were collected from the bowl followed by pre-sintering at 700°C for 3 h and ground in a mortar–pestle setup to ensure a fine powder. The ground powders were mixed with polyvinyl alcohol (4 wt.%), then placed in a hydraulic press machine under a pressure of 3±0.5 MPa for 1 min to form pellet and toroid shapes and finally sintered at 1050°C, 1100°C and 1150°C for 4 h.

2.2. *Characterization*

The structural pattern was characterized by powder X-ray diffraction (PXRD; EMMA, GBC Scientific Equipment) radiation functioned at 40 kV and 40 mA, while the source was Cu-Kα (λ=1.54052 Å). Infrared spectra were measured by Fourier Transform Infrared Spectrometer (FTIR; Frontier, PerkinElmer) and the surface morphology was analyzed by Scanning Electron Microscope (SEM; S3400N, Hitachi) functioned at 15 kV. The magnetic properties were studied by Vibrating Sample Magnetometer (VSM; EV-6, MicroSense) at room temperature. Dielectric parameters were measured by a high-precision impedance analyzer (4294A, Agilent) within the frequency range from 40 Hz to 110 MHz and reflectance data were collected by UV–vis–NIR spectrophotometer (UV-2600, Shimadzu).

3. Results and Discussion

3.1. *Structural analyses*

The structure of $Ni_{0.08}Mn_{0.90}Zn_{0.02}Fe_2O_4$ ferrite was determined by powder XRD with a step size of 0.02°, where the diffraction angle (2θ) ranges from 20° to 70°. The appearances of (220), (311), (222), (400), (422), (511) and (440) planes at the diffraction angle in Fig. 1(a) confirm the formation of cubic spinel structure without any phase impurity and a good coherence to our earlier report.[22] The average crystallite sizes (τ) were calculated by using the Debye–Scherrer formula from the highest intensity peak near 36° (diffraction angle, 2θ) associated with the (311) plane,[23]

$$\tau = \frac{K\lambda}{\beta\cos\theta}, \tag{1}$$

where K, λ and β are the shape factor, incident X-ray wavelength and FWHM (rad), respectively.

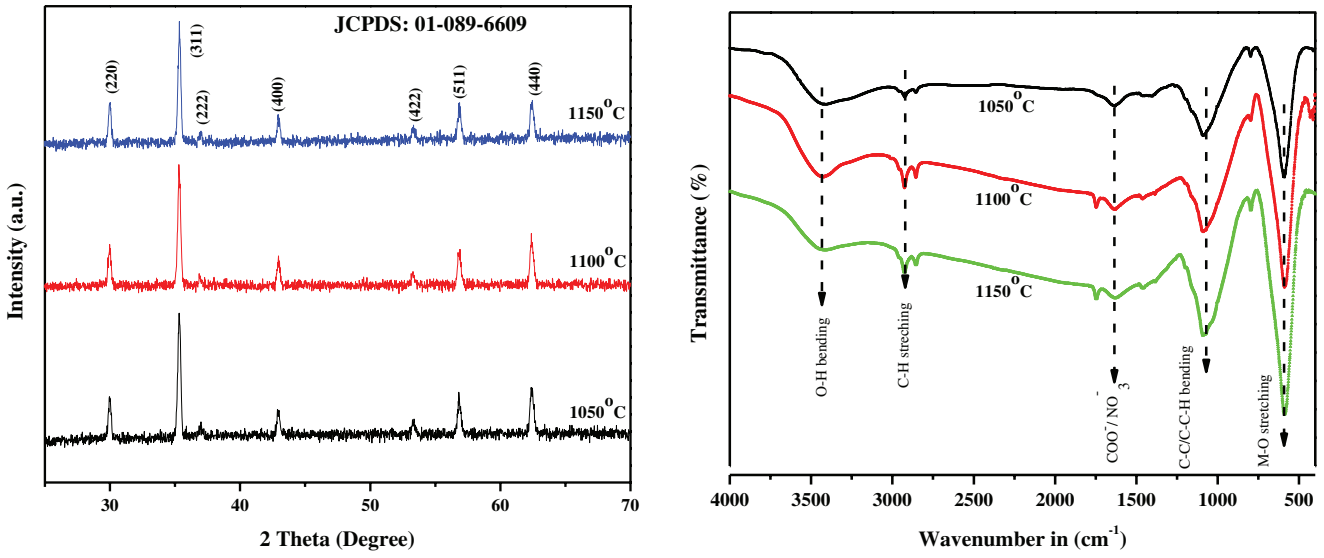

(a) (b)

Fig. 1. (a) XRD patterns and (b) FTIR absorption bands of $Ni_{0.08}Mn_{0.90}Zn_{0.02}Fe_2O_4$ ferrite.

The crystal size has been found to increase when the sintering temperature rises. This is because the sintering process generally reduces the lattice defects and strain, resulting in a lump of smaller grains and hence an increase in the average grain size.[24] The X-ray density was found to be greater than the bulk density which may occur from the microcrack and lattice vacancy during the sintering process as these defects can be precisely quantified through XRD spectra than mass density measurement.[25] The porosity P (%) of the samples that was calculated from X-ray density and bulk density has experienced a decreasing trend due to densification with the increase of the sintering temperature (Table 1). The heat energy creates a force that interacts with grain boundaries which clothes the pores resulting in the reduction of porous area and hence a highly compact material is formed throughout the sintering process.[26] Some other parameters like hopping length, tetrahedral and octahedral bond lengths, etc. were calculated from the experimental lattice parameter and listed in Table 2.

3.2. *FTIR analyses*

Figure 1(b) exhibits the FTIR spectra (T%) of the prepared powders in the wavenumber range of 400–4000 cm^{-1}.

Table 1. Variations of the lattice parameter a, crystalline size t, X-ray density d_x, bulk density d_B, porosity P, frequency bands (ν_1 and ν_2) and force constants [octahedral sites (K_o) and tetrahedral sites (K_t)] of $Ni_{0.08}Mn_{0.90}Zn_{0.02}Fe_2O_4$ ferrite.

Temperature (°C)	a (Å)	t (nm)	d_x (g/cm^3)	d_B (g/cm^3)	P (%)	ν_1 (cm^{-1})	ν_2 (cm^{-1})	K_o (×10^5 dyn·cm^{-2})	K_t (×10^5 dyn·cm^{-2})
1050	8.41821	23.18	5.1442	4.62	10.19	582	436	1.60	3.03
1100	8.41971	23.05	5.1469	4.80	6.74	589	412	1.43	2.90
1150	8.41519	23.81	5.1525	4.89	5.09	582	429	1.55	2.98

Table 2. The calculated values of hopping lengths between the magnetic ions in the tetrahedral (A) and octahedral (B) sites (L_A and L_B), tetrahedral bond length (d_{AX}), octahedral bond length (d_{BX}), tetrahedral edge (d_{AXE}), sheared octahedral edge (d_{BXE}), unsheared octahedral edge (d_{BXEU}), A-site radius (r_A) and B-site radius (r_B) of $Ni_{0.08}Mn_{0.90}Zn_{0.02}Fe_2O_4$ ferrite.

Temperature (°C)	Hopping lengths								
	L_A (Å)	L_B (Å)	d_{AX} (Å)	d_{BX} (ÅÅ)	d_{AXE} (Å)	d_{BXE} (Å)	d_{BXEU} (Å)	r_A (Å)	r_B (Å)
1050	3.6451	2.9762	1.9100	2.0552	3.1191	2.8334	2.9780	0.5900	0.7340
1100	3.6458	2.9768	1.9104	2.0556	3.1197	2.8339	2.9785	0.5904	0.7344
1150	3.6438	2.9752	1.9093	2.0545	3.1180	2.8324	2.9769	0.5893	0.7333

Ferrite exhibits a similar structure to spinel $MgAl_2O_3$ having the space group of *Fd*3*m*. An equipotential force makes ferrite as an incessant bonded crystal with atoms coupled to all their adjacent neighbors.[27] In the case of solid crystal, the infrared spectrum can be attributed to the vibration of ions within the wavelength range from 300 cm^{-1} to 4000 cm^{-1}. The spectrum reveals two significant absorption peaks under 1000 cm^{-1} which is a trademark of all single-phase spinel ferrites. The high-frequency band (ν_1) lying at 582–589 cm^{-1} is associated with intrinsic stretching vibrations of Fe^{2+}–O at the tetrahedral *A*-site, while the low-frequency band (ν_2) lying at 429–436 cm^{-1} is due to stretching vibrations of Fe^{2+}–O at the octahedral *B*-site. The values of these two bands differ upon the change in the stretching length of Fe–O in the *A*- and *B*-site lattices.[28,29]

3.3. *Morphology study*

SEM has been applied to determine the microstructural images of $Ni_{0.08}Mn_{0.90}Zn_{0.02}Fe_2O_4$ ferrite and the results are shown in Fig. 2. The average grain sizes were determined from the SEM micrographs by linear intercept technique from the ImageJ software; the size extends from 0.27 μm to 0.88 μm, as listed in Table 3. It seems a cluster of grains was formed at 1050°C, whereas the sharp notch-type grains were developed at 1100°C and 1150°C. It was also observed that as the sintering temperature was raised the grain size increased. This may be attributed to the development of crystallinity steered by temperature, which causes a growing number of crystallites.[4]

3.4. *Room-temperature magnetic properties*

Figure 3 depicts the room-temperature hysteresis curves of the prepared samples that were acquired from VSM with a maximum applied field of ±20 kOe. Some magnetic properties like coercivity (H_c), saturation magnetization (M_s), remanent magnetization (M_r), Bohr magnetons (μ_B) and remanence ratio (M_r/M_s) were measured from the *M*–*H* curve, and compiled in Table 3. Both magnetons number and anisotropy constant increased with increasing sintering temperature,

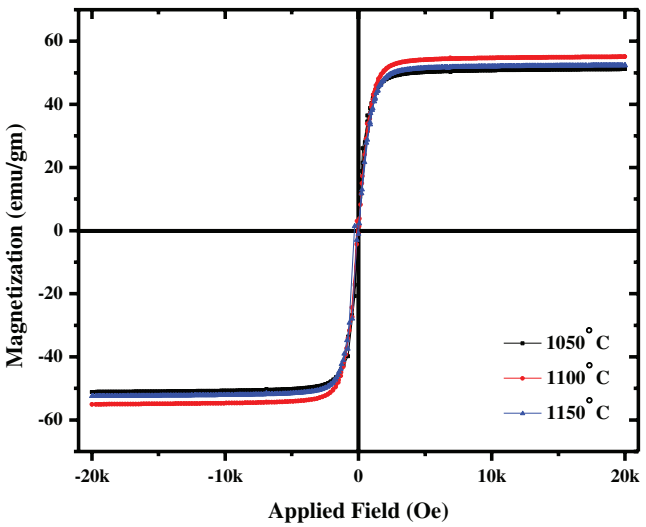

Fig. 3. Room-temperature magnetic hysteresis loops of $Ni_{0.08}Mn_{0.90}Zn_{0.02}Fe_2O_4$ ferrite.

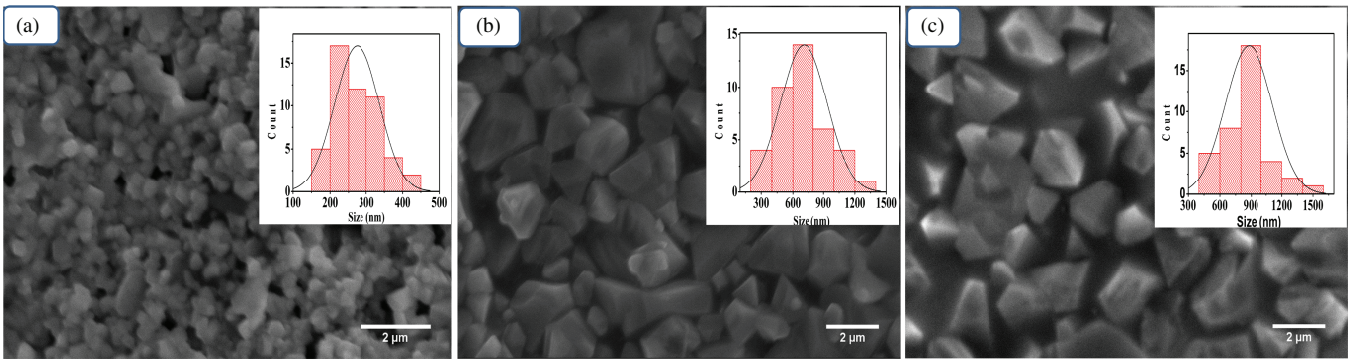

Fig. 2. SEM images of the $Ni_{0.08}Mn_{0.90}Zn_{0.02}Fe_2O_4$ ferrite sintered at (a) 1050°C, (b) 1100°C and (c) 1150°C.

Table 3. Magnetic parameters of $Ni_{0.08}Mn_{0.90}Zn_{0.02}Fe_2O_4$ ferrite at different sintering temperatures.

Sintering temperature (°C)	Average grain size (μm)	M_s (emu/g)	M_r (emu/g)	H_c (Oe)	(M_r/M_s)	Magnetic moment/ formula unit (n_B)	Anisotropy constant (erg/g)
1050	0.27	51.16	16.02	26.31	0.31	2.12	1402.10
1100	0.71	55.02	11.58	19.52	0.21	2.28	1118.74
1150	0.88	52.39	8.64	30.43	0.16	2.17	1660.65

owing to an increase in the *A–B* interaction, as estimated by the following expressions[30]:

$$\text{Bohr magnetons}\,(\mu_B) = \frac{(M_s \times \text{mole weight})}{5585}, \quad (2)$$

$$\text{Anisotropy constant} = \frac{H_c \times M_s}{0.96}. \quad (3)$$

All samples have shown a narrow hysteresis loop (H_c~19.52–30.43 Oe), which indicates the formation of soft ferrite. For all samples, the M_s value was derived using the law of approach to saturation, which increases as the grain size increases.[31] This trend is consistent with Ref. 32. A slight improvement of saturation magnetization (M_s) can be obtained from 51.16 emu/g (0.27 μm) to 52.39 emu/g (0.88 μm), while the estimated theoretical value of M_s for bulk Fe_2O_3 is about 92 emu/g.[33] Grain size has an impact on coercivity and remanent magnetization, as listed in Table 3. Both H_c and M_r increase with the grain size. In the case of soft ferrite, high spin interaction in the finely crystalline Fe_2O_3 particles throughout spin orientation may result in the high value of H_c.[34] Because of the presence of super-exchange couplings, such consequences are more significant in the case of ferrites. Following Neel's ferromagnetism model, the cations on different sublattices (tetrahedral and octahedral sites) in the spinel crystals exhibit magnetic moments that are inversely oriented. Hence, the magnetic moment per formula unit (n_B; in μ_B) is: $n_B = M_{oct} - M_{tet}$, where M_{oct} and M_{tet} are the magnetic moments of the octahedral and tetrahedral sites, respectively. With the increase in sintering temperature, migration of Fe^{3+} ions increases from tetrahedral *A*-site to octahedral *B*-site. This causes the *B*-site magnetization to increase and that of *A*-site to decrease, resulting in an increase in the net magnetization.[35,36] In addition, higher calcination temperature allows wider grain growth with less crystalline defect, resulting in a higher magnetization value.[37]

3.5. *Permeability study*

The permeability of polycrystalline ferrites is associated with two types of magnetic modes; spin resonance and domain wall motion.[38] Permeability is predominated by domain wall motion at low frequency in contrast to spin resonance.[39] It is notable that initial permeability may be enhanced by using optimal chemical formulations, highly packed microstructures and wider-shape grains with narrow borders.[40] The frequency-dependent real part of initial permeability (μ') at different temperatures [Fig. 4(a)] shows a decreasing trend at the lower-frequency zone, while possessing the maximum value at higher-frequency region and followed by a sudden decrease at 100 MHz. This may due to the diverse nature of the relaxation resonance phenomena.[41] As the domain wall motion increases with temperature, hence permeability (μ') also increases with the sintering temperature. This occurs because the density and grain size increase with increasing sintering temperature as previously described.

3.6. *DC electrical resistivity*

The DC electrical resistivities for all the samples were determined as a function of temperature employing the two-probe technique. Figure 4(b) shows the plot of DC resistivity of the samples versus 1000/*T*. The electrical resistivity reduces as the temperature rises, revealing the semiconducting nature of the samples. The values of Curie temperature (T_c), resistivity

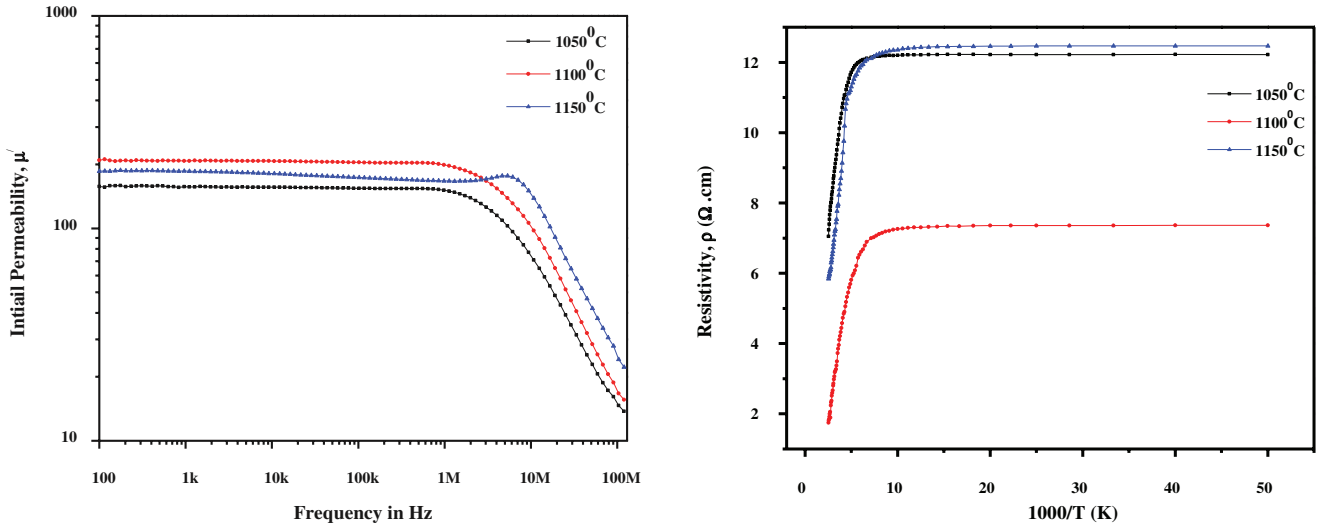

Fig. 4. (a) Frequency versus initial permeability and (b) 1000/*T* versus resistivity plots of $Ni_{0.08}Mn_{0.90}Zn_{0.02}Fe_2O_4$ ferrite.

Table 4. Curie temperature, activation energy and resistivity values of $Ni_{0.08}Mn_{0.90}Zn_{0.02}Fe_2O_4$ ferrite at room temperature.

Sintering temperature (°C)	T_c (°C)	Resistivity at room temperature ($\times 10^7\ \Omega$·cm)	Activation energy (eV)
1050	200	20.20	0.082
1100	165	1.62	0.109
1150	160	0.24	0.491

at room temperature and the activation energy (ΔE_a) that were calculated from the slopes of the linear plots of DC resistivity for all the samples, are stated in Table 4. It seems DC electrical resistivity decreases as the sintering temperature rises. This may be due to the formation of bigger grains at higher sintering temperatures. Larger grains mean more grain-to-grain contact area for electron flow and, as a result, a lower barrier height.[42] The nature of Curie temperature is influenced by the crystal defect, microstructural formation, grain size, porous nature, etc.[43] It is found that with increasing sintering temperature, T_c decreases. Such kind of variation in T_c is related to the internal stress which can raise the free energy of the ferroelectric phase and reduce the Curie temperature. A large number of pores reduces the internal stress; therefore, ferrites with a relatively lower density may yield a larger T_c value than denser form.[44] The ΔE_a values of the samples ranged from 0.082 eV to 0.491 eV, suggesting that the conduction process is owing to the hopping of charge carriers consistent with Ref. 45.

3.7. *Frequency dispersion dielectric analyses*

Dielectric analyses were carried out within the frequency range of 100 Hz–1 MHz with a high-precision impedance analyzer. Figure 5(a) reveals that the dielectric constants ($\acute{\varepsilon}$)

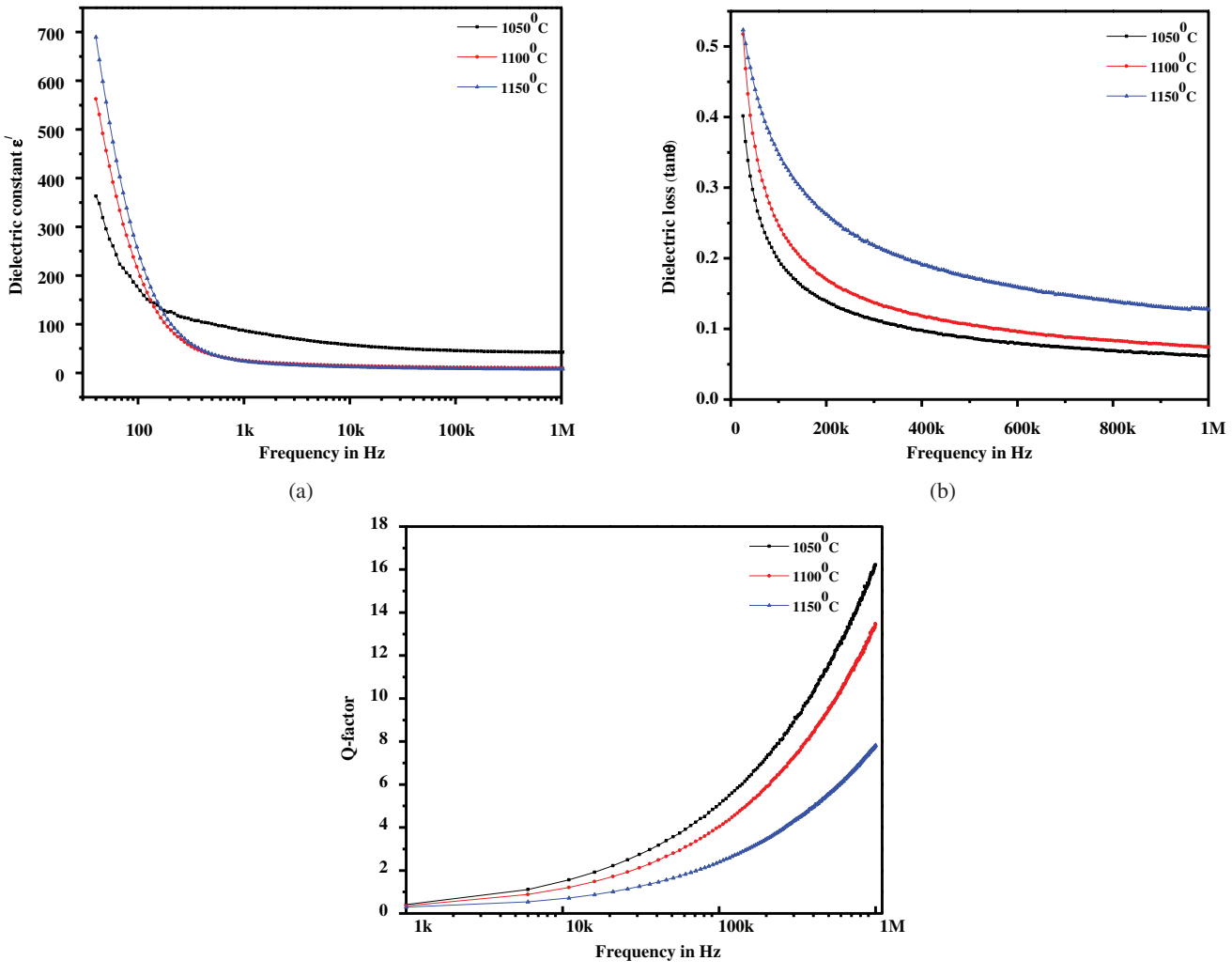

Fig. 5. Variations of (a) dielectric constant ($\acute{\varepsilon}$), (b) dielectric loss (tan δ) and (c) Q-factor as a function of frequency of the $Ni_{0.08}Mn_{0.90}Zn_{0.02}Fe_2O_4$ ferrite.

of all samples decreased with increasing frequency, indicating a normal ferromagnetic behavior. This behavior may be explained by Maxwell–Wagner type polarization and Koop's theory.[46,47] Ionic, electronic, interfacial, dipolar polarizations, etc. are associated with dielectric constants which greatly dominate the dielectric properties. Initially, electrons are well aligned with the applied field and flocked at grain boundaries via hopping, resulting in polarization. However, at a certain frequency, the electron exchange between Fe^{2+} and Fe^{3+} ions cannot follow the applied field since it takes a limited time to align with the field direction that declines the polarization as well as the dielectric constant.[48]

The dielectric loss also decreases (tan δ) with frequency similar to the dielectric constant ($\acute{\varepsilon}$), as shown in Fig. 5(b). This decrease takes place when the jumping frequency of electric charge carriers cannot follow the alteration of the applied AC electric field beyond a certain critical frequency.[49] The maximum tanδ value is displayed at 25 kHz, whereas the minimum value is found at 1 MHz. Dielectric loss tangent showed higher values for higher sintering temperatures. It may be due to the fact that by increasing the sintering temperature, grain size increased.[50] It is assumed that the grains are relatively more conducting as compared to the grain boundary layers which results in the decrease in grain boundary layer thickness as the grain size increases. This implies that the effective capacitance of the sample would increase with increasing grain size. As a result, the overall dielectric loss of the ferrites increases with increasing grain size.[51] The Q-factor of all samples increased with increasing frequency, as shown in Fig. 5(c), which can be attributed to ferromagnetic resonance losses.[52] It is observed that the sample sintered at 1050°C exhibited the highest Q-factor.

3.8. *Optical investigation*

Room-temperature Kubelka–Munk functions [$F(R_\infty)$] of $Ni_{0.08}Mn_{0.90}Zn_{0.02}Fe_2O_4$ ferrite have been derived from diffuse reflectance spectroscopy (DRS) within the wavelength spectrum of 220–1400 nm by using a UV–vis–NIR spectrometer. Diffuse reflectance spectra are a better choice for analyzing the optical characteristics of powdered materials as they exhibit little scattering effects, unlike the UV absorption spectra. All of the samples absorb energy in the region of 500–600 nm, as seen in Fig. 6. The optical bandgap (E_g) can be estimated by the Tauc plot of the Kubelka-Munk function as

$$F(R_\infty) = \frac{(1-R_\infty)^2}{2R_\infty}, \tag{4}$$

where R_∞ is the diffuse reflectance.

The Kubelka–Munk function commonly deals with powder samples as it transforms the diffused reflectance analogous to absorption coefficient. As a result, Tauc's relationship may be expressed as: $F(R_\infty) \times h\nu = A(h\nu - E_g)^n$, where A and n are the proportionality constant and transition coefficient,

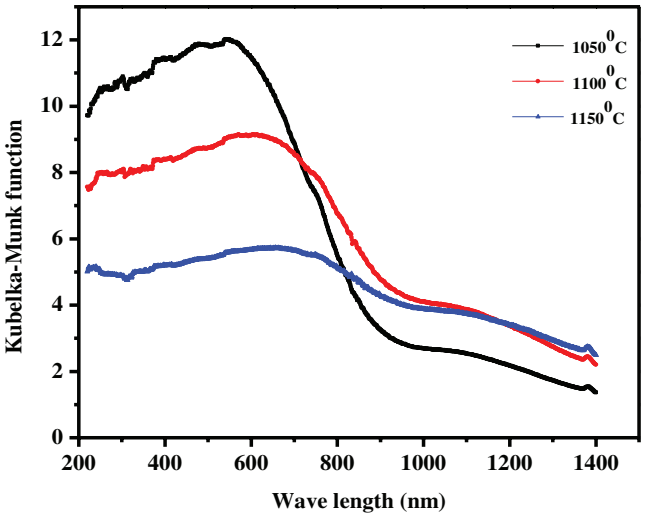

Fig. 6. Kubelka–Munk functions of $Ni_{0.08}Mn_{0.90}Zn_{0.02}Fe_2O_4$ ferrite.

respectively. For direct bandgap n=1/2, while for indirect bandgap n = 2. The optical bandgap for directly allowed transition (n = 1/2) of $Ni_{0.8}MnZn_{0.2}Fe_2O_4$ ferrite is estimated from the extrapolation slope of Tauc plot of $F(R_\infty) \times h\nu$ versus photon energy, while the value of $F(R_\infty) \times h\nu$ is equal to zero at the x-axis intercept. Figure 7 shows the band energy (E_g) for the prepared $Ni_{0.08}Mn_{0.90}Zn_{0.02}Fe_2O_4$ ferrite varying

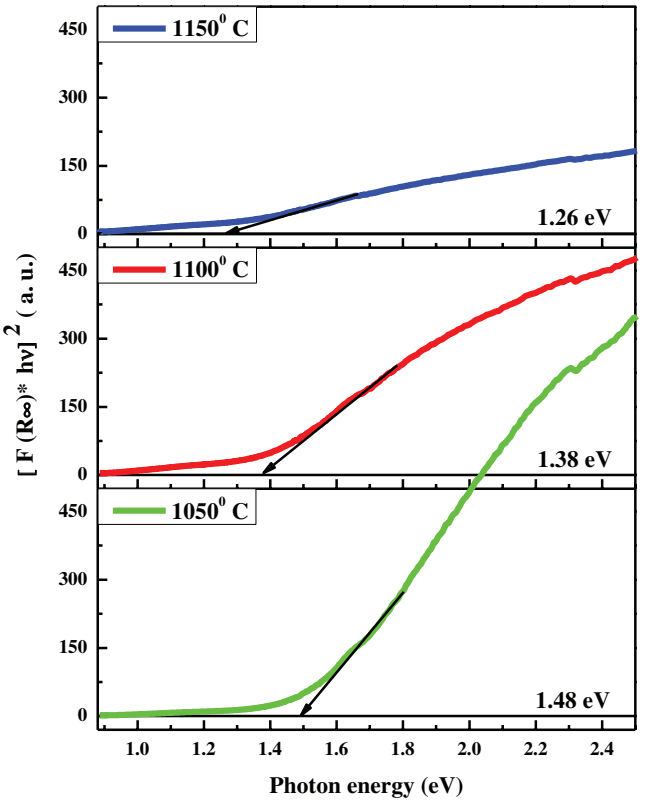

Fig. 7. Optical bandgaps of $Ni_{0.08}Mn_{0.90}Zn_{0.02}Fe_2O_4$ ferrite.

from 1.26 eV to 1.48 eV at different sintering temperatures. It seems the band energy decreased with sintering temperature which may be due to the increase in particle size.[53]

4. Conclusion

Polycrystalline $Ni_{0.08}Mn_{0.90}Zn_{0.02}Fe_2O_4$ ferrite was successfully prepared by a conventional ceramic method and the influence of sintering temperature on its structural, magnetic, optical and frequency-dependent electrical and dielectric properties has been investigated. All the samples confirmed the single-phase cubic spinel structure that matches well with the FTIR spectra. The average grain size and density increased with sintering temperature. Both the Curie temperature and DC electrical resistivity of the samples decreased with increasing grain size. The dielectric constant and loss tangent were studied as a function of frequency and temperature. It was found that both the parameters decreased with frequency. The sample sintered at 1150°C showed a high dielectric constant as well as dielectric loss. Low coercivity was observed at 1100°C (~19 Oe) which allows its application in transformer cores and multilayer chip inductors (MLCIs).

Acknowledgments

The authors are grateful to the Bangladesh Council of Scientific and Industrial Research (BCSIR) authority for providing the grant to carry out this research work. They were also thankful to all the scientists and staff of the Industrial Physics Division, BCSIR Laboratories, Dhaka for their co-operation.

References

[1]A. Sutka, G. Mezinskis and A. Lusis, Electric and dielectric properties of nanostructured stoichiometric and excess-iron Ni–Zn ferrites, *Phys. Scr*. **87**, 025601 (2013).

[2]Z. Z. Lazarevic, C. Jovalekic, A. Milutinovic, D. Sekulic, V. N. Ivanovski, A. Recnik, B. Cekic and N. Z. Romcevic, Nanodimensional spinel $NiFe_2O_4$ and $ZnFe_2O_4$ ferrites prepared by soft mechanochemical synthesis, *J. Appl. Phys*. **113**, 187221 (2013).

[3]M. Shahjahan, N. A. Ahmed, S. N. Rahman, S. Islam, N. Khatun and M. S. Hossain, Structural and electrical characterization of Li-Zn ferrites, *Int. J. Innov. Technol. Explor. Eng.* **3**, 48 (2014).

[4]M. S. Hossain, M. B. Alam, M. Shahjahan, M. H. A. Begum, M. Hossain, S. Islam, N. Khatun, M. S. Alam and M. A. Mamun, Synthesis, structural investigation, dielectric and magnetic properties of Zn^{2+} doped cobalt ferrite by the sol–gel technique, *J. Adv. Dieletr.* **08**, 1850030 (2018).

[5]K. Praveena, K. Sadhana, S. Matteppanavar and H. L. Liu, Effect of sintering temperature on the structural, dielectric and magnetic properties of $Ni_{0.4}Zn_{0.2}Mn_{0.4}Fe_2O_4$ potential for radar absorbing, *J. Magn. Magn. Mater.* **423**, 343 (2017).

[6]P. Thakur, D. Chahar, S. Taneja, N. Bhalla and A. Thakur, A review on MnZn ferrites: Synthesis, characterization and applications, *Ceram. Int.* **46**, 15740 (2020).

[7]W. Wang, C. Zang and Q. Jiao, Synthesis, structure and electromagnetic properties of Mn-Zn ferrite by sol-gel combustion technique, *J. Magn. Magn. Mater.* **349**, 116 (2014).

[8]J. T. Jang, H. Nah, J. H. Lee, S. H. Moon, M. G. Kim and J. Cheon, Critical enhancements of MRI contrast and hyperthermic effects by dopant-controlled magnetic nanoparticles, *Angew. Chem., Int. Ed.* **48**, 1234 (2009).

[9]M. I. A. A. Maksoud, G. S. El-Sayyad, A. M. El-Khawaga, M. A. Elkodous, A. Abokhadra, M. A. Elsayed, M. Gobara, L. I. Soliman, H. H. El-Bahnasawy and A. H. Ashour, Nanostructured Mg substituted Mn-Zn ferrites: A magnetic recyclable catalyst for outstanding photocatalytic and antimicrobial potentials, *J. Hazard. Mater.* **399**, 12300 (2020).

[10]A. Hajalilou, M. Hashim and H. M. Kamari, Effects of additives and sintering time on the microstructure of Ni-Zn ferrite and its electrical and magnetic properties, *Adv. Mater. Sci. Eng.* **2014**, 138789 (2014).

[11]G. Ott, J. Wrba and R. Lucke, Recent developments of Mn–Zn ferrites for high permeability applications, *J. Magn. Magn. Mater*. **254–255**, 535 (2003).

[12]U. Ghazanfar, S. A. Siddiqi and G. Abbas, Structural analysis of the Mn–Zn ferrites using XRD technique, *J. Mater. Sci. Eng. B* **118**, 84 (2005).

[13]A. K. Singh, T. C. Goel and R. G. Mendiratta, Dielectric properties of Mn-substituted Ni-Zn ferrites, *J. Appl. Phys.* **91**, 6626 (2002).

[14]S. T. Mahmud, A. K. M. Akther Hossain, M. A. Hakim, M. Seki, T. Kawai and H. Tabata, Influence of microstructure on the complex permeability of spinel type Ni–Zn ferrite, *J. Magn. Magn. Mater*. **305**, 269 (2006).

[15]N. A. Ahmed, M. Shahjahan, S. M. Talukder, M. S. Hossain, M. H. A. Begum, R. L. Warnock, M. A. Haque and M. Hossain, Synthesis and characterization of structural, and electrical properties of $Mg(0.25x)Cu(0.25x)Zn(1–0.5x)Fe_2O_4$ ferrites by sol-gel method, *Ukr. J. Phys.* **64**, 861 (2019).

[16]K. Huang, X. Liu, S. Feng, J. Yu, X. Niu, F. Lv and X. Huang, Structural and magnetic properties of Cr-substituted NiCuZn ferrite, *High Temp. Mater. Process.* **35**, 531 (2016).

[17]A. Gadkari, T. Shinde and P. V. Mbekar, Influence of rare-earth ions on structural and magnetic properties of $CdFe_2O_4$ ferrites, *J. Rare Met.* **29**, 168 (2010).

[18]M. Sinha and S. K. Pradhan, Synthesis of nanocrystalline Cd–Zn ferrite by ball milling and its stability at elevated temperatures, *J. Alloys Compd.* **489**, 91 (2010).

[19]M. S. Hossain, Y. Akter, M. Shahjahan, M. S. Bashar, M. H. A. Begum, M. M. Hossain, S. Islam, N. Khatun and M. Al-Mamun, Influence of Ni substitution on structural, morphological, dielectric, magnetic and optical properties of Cu-Zn ferrite by double sintering sol-gel technique, *J. Adv. Dieletr*. **09**, 1950020 (2019).

[20]A. K. Singh, A. Verma, O. P. Thakur, C. Prakash, T. C. Goel and R. G. Mendiratta, Electrical and magnetic properties of Mn–Ni–Zn ferrites processed by citrate precursor method, *Mater. Lett.* **57**, 1040 (2003).

[21]P. Pulisova, J. Kovac, A. Voigt and P. Raschman, Structure and magnetic properties of Co and Ni nano-ferrites prepared by a two step direct microemulsions synthesis, *J. Magn. Magn. Mater.* **341**, 93 (2013).

[22]M. H. A. Begum, N. Khatun, S. Islam, N. A. Ahmed, M. S. Hossain, M. A. Gafur and A. Siddika, Synthesis and characterization of structural, magnetic and electrical properties of Ni–Mn–Zn ferrites, *Int. J. Nanoelectron. Mater.* **11**, 15 (2018).

[23]M. George, S. S. Nair, K. A. Malini, P. A. Joy and M. R. Anantharaman, Finite size effects on the electrical properties of sol–gel synthesized $CoFe_2O_4$ powders: Deviation from Maxwell–Wagner theory and evidence of surface polarization effects, *J. Phys. D, Appl. Phys.* **40**, 1593 (2006).

[24]T. P. Raming, A. J. A. Winnubust, C. M. Van Kats and A. P. Philipse, The synthesis and magnetic properties of nanosized hematite (α-Fe_2O_3) particles, *J. Colloid Interface Sci.* **249**, 346 (2002).

[25]S. C. Mazumdar, A. T. Traina, M. J. Miah and M. I. Khan, Effect of Sr-substitution on the structural and magnetoelectric properties of Ni-Zn ferrites, *Bang. J. Phys.* **26**, 1 (2019).
[26]F. F. Lange and B. J. Kellett, Thermodynamics of densification: II, Grain growth in porous compacts and relation to densification, *J. Am. Ceram. Soc.* **72**, 735 (1989).
[27]S. Mirzaee, Y. Azizian-Kalandaragh and P. Rahimzadeh, Modified co-precipitation process effects on the structural and magnetic properties of Mn-doped nickel ferrite nanoparticles, *Solid State Sci.* **99**, 106052 (2020).
[28]M. Kaiser, Effect of nickel substitutions on some properties of Cu-Zn ferrites, *J. Alloys. Compd.* **468**, 15 (2009).
[29]R. D. Waldron, Infrared spectra of ferrites, *Phys. Rev.* **99**, 1727 (1955).
[30]R. C. Kambale, P. A. Shaikh, S. S. Kamble and Y. D. Kolekar, Effect of cobalt substitution on structural, magnetic and electric properties of nickel ferrite, *J. Alloys Compd.* **478**, 599 (2009).
[31]M. Klokkenburg, C. Vonk, E. M. Claesson, J. D. Meeldijik, B. H. Erne and A. P. Philipse, Direct imaging of zero-field dipolar structures in colloidal dispersions of synthetic magnetite, *J. Am. Chem. Soc.* **126**, 51 (2004).
[32]Q. Li, C. W. Kartikowati, S. Horie, T. Ogi, T. Iwaki and K. Okuyama, Correlation between particle size/domain structure and magnetic properties of highly crystalline Fe_3O_4 nanoparticles, *Sci. Rep.* **7**, 9894 (2017).
[33]G. F. Goya, T. S. Berquó, F. C. Fonseca and M. P. Morales, Static and dynamic magnetic properties of spherical magnetite nanoparticles, *J. Appl. Phys.* **94**, 3520 (2003).
[34]G. Herzer, Nanocrystalline soft magnetic materials, *J. Magn. Magn. Mater.* **112**, 258 (1992).
[35]Y. B. Kannan, R. Saravanan, N. Srinivasan and I. Ismail, Sintering effect on structural, magnetic and optical properties of $Ni_{0.5}Zn_{0.5}Fe_2O_4$ ferrite nano particles, *J. Magn. Magn. Mater.* **423**, 217 (2017).
[36]K. Rana, P. Thakur, P. Sharma, M. Tomar, V. Gupta and A. Thakur, Improved structural and magnetic properties of cobalt nanoferrites: Influence of sintering temperature, *Ceram. Int.* **41**, 4492 (2014).
[37]H. R. Lakshmiprasanna, V. J. Angadi, B. R. Babu, M. Pasha, K. Manjunatha and S. Matteppanavar, Effect of Pr^{3+}-doping on the structural, elastic and magnetic properties of Mn–Zn ferrite nanoparticles prepared by solution combustion synthesis method, *Chem. Data Collect*. **24**, 100273 (2019).
[38]T. Nakamura, Low-temperature sintering of Ni–Zn–Cu ferrite and its permeability spectra, *J. Magn. Magn. Mater.* **168**, 285 (1997).
[39]M. R. Barati, Characterization and preparation of nanocrystalline MgCuZn ferrite powders synthesized by sol–gel auto-combustion method, *J. Sol-Gel Sci. Technol.* **52**, 171 (2009).
[40]J. Kalarus, G. Kogias, D. Holz and V. T. Zaspalis, High permeability–high frequency stable MnZn ferrites, *J. Magn. Magn. Mater.* **324**, 2788 (2012).
[41]G. Herrera, Domain wall dispersions: Relaxation and resonance in Ni–Zn ferrite doped with V_2O_5, *J. Appl. Phys*. **108**, 103901 (2010).
[42]E. M. M. Ibrahim, The effect of sintering time and temperature on the electrical properties of MnZn ferrites, *Appl. Phys. A* **89**, 203 (2007).
[43]H. Su, H. Zhang, X. Tang and X. Xiang, High-permeability and high-Curie temperature NiCuZn ferrite, *J. Magn. Magn. Mater*. **283**, 157 (2004).
[44]X. M. Chen, H. Y. Ma, W. Ding, Y. Zhang, X. G. Zhao, X. Liang and P. Liu, Microstructure, dielectric, and piezoelectric properties of $Pb_{0.92}Ba_{0.08}Nb_2O_{6-0.25}$ wt% TiO_2 ceramics: Effect of sintering temperature, *J. Am. Ceram. Soc.* **94**, 3364 (2011).
[45]M. T. Hossain, S. Islam, M. H. Mondal and A. H. Khan, Studies on anomalous behavior at curie point T_c of some classes of mixed ferrites, *Bang. J. Sci. Ind. Res.* **41**, 171 (2006).
[46]*C. G.* Koops, On the dispersion of resistivity and dielectric constant of some semiconductors at audio frequencies, *Phys*. *Rev*. *B* **83**, 121 (1951).
[47]K. W. Wagner, The distribution of relaxation times in typical dielectrics, *Ann. Phys.* **40**, 817 (1973).
[48]K. Radha and D. Ravinder, Frequency and composition dependence of dielectric behavior of mixed Li-Cd ferrite, *Indian J. Pure Appl. Phys.* **33**, 74 (1995).
[49]P. Hu, H. Yang, D. Pan, H. Wang, J. Tian, S. Zhang, X. Wang and A. A. Volinsky, Heat treatment effects on microstructure and magnetic properties of Mn-Zn ferrite powders, *J. Magn. Magn. Mater.* **322**, 173 (2010).
[50]M. Hanif, U. Rafiq, M. Anis-ur-Rehman and A. Ul Haq, Structural and dielectric properties of rare earth doped lithium nanoferrites for sensing applications, *J. Supercond. Nov. Magn.* **30**, 3573 (2017).
[51]K. V. R. Prasad, A. R. Raju and K. B. R. Varma, Grain size effects on the dielectric properties of ferroelectric $Bi_2VO_{5.5}$ ceramics, *J. Mater. Sci.* **29**, 2691 (1994).
[52]M. M. Haque, M. Huq and M. A. Hakim, Influence of CuO and sintering temperature on the microstructure and magnetic properties of Mg–Cu–Zn ferrites, *J. Magn. Magn. Mater.* **320**, 2792 (2008).
[53]T. M. Hammad, J. K. Salem, A. A. Amsha and N. K. Hejazy, Optical and magnetic characterizations of zinc substituted copper ferrite synthesized by a co-precipitation chemical method, *J. Alloys Compd.* **741**, 123 (2018).